Ultraviolet-Durable Flexible Nonfullerene Organic Solar Cells Realized by a Hybrid Nanostructured Transparent Electrode

Xu, Tao; Gong, Chunliu; Wang, Shuanglong; Lian, Hong; Lan, Weixia; Lévêque, Gaëtan; Grandidier, Bruno; Plain, Jerôme; Bachelot, Renaud; Wei, Bin; Zhu, Fu Rong

Published in:
Solar RRL

DOI:
10.1002/solr.201900522

Published: 01/05/2020

Document Version:
Peer reviewed version

Ultraviolet Durable Flexible Nonfullerene Organic Solar Cells Realized by a Hybrid Nanostructured Transparent Electrode

Tao Xu[1], Chunliu Gong[1], Shuanglong Wang[1], Hong Lian[1], Weixia Lan[1*], Gaëtan Lévêque[2], Bruno Grandidier[2], Jerôme Plain[3], Renaud Bachelot[3], Bin Wei[1*], Furong Zhu[4*]

[1.] School of Mechatronic Engineering and Automation, Key Laboratory of Advanced Display and System Applications, Ministry of Education, Shanghai University, 200072, Shanghai, China

[2.] IEMN, UMR8520, Université de Lille 1, 59652 Villeneuve d'Ascq Cédex, France

[3.] Light, nanomaterials, nanotechnologies (L2n) Laboratory. Charles Delaunay Institute, CNRS. University of Technology of Troyes, 12 rue Marie Curie, F-10004 Troyes Cedex, France

[4.] Department of Physics, Research Centre of Excellence for Organic Electronics and Institute of Advanced Materials, Hong Kong Baptist University, Kowloon Tong, Hong Kong, China

Corresponding Author

Email: weixia_lan@shu.edu.cn, bwei@shu.edu.cn, frzhu@hkbu.edu.hk

A significant enhancement in ultraviolet (UV) durable indium tin oxide (ITO)-free flexible nonfullerene organic solar cells (OSCs) has been demonstrated using a hybrid nanostructured flexible transparent electrode (FTE), comprising a mixture of 0D silver nanoparticles (AgNPs), 1D Ag nanowires (AgNWs) and 2D exfoliated graphene sheets. The FTE possesses high optical transparency and electric conductivity, good air stability and full-solution fabrication capability at a low processing temperature. An average power convention efficiency (PCE) of 8.15% has been obtained for the flexible nonfullerene OSCs, based on the blend of poly[(2,6-(4, 8-bis(5-(2-ethylhexyl)thiophen-2-yl)-benzo[1,2-b:4,5-b']dithiophene))-alt-(5,5-(1',3'-di-2-thienyl-5',7'-bis(2-ethylhexyl)benzo[1',2'-c:4',5'-c'] dithiophene-4,8-dione)] (PBDB-T): 3,9-bis(2-methylene-(3-(1,1-dicyanomethylene)-indanone))-5,5,11,11-tetrakis(4-hexylphenyl)-dithieno[

This article has been accepted for publication and undergone full peer review but has not been through the copyediting, typesetting, pagination and proofreading process, which may lead to differences between this version and the Version of Record. Please cite this article as doi: 10.1002/solr.201900522.

2,3-d:2',3'-d']-s-indaceno[1,2-b:5,6-b'] dithiophene (ITIC). The flexible PBDB-T:ITIC OSCs exhibit an excellent UV durability compared to the ITO-based control cell, realized by incorporating a FTE with a tailored absorption in wavelength < 380 nm. The novel FTE developed in this work provides a promising alternative to ITO for use in UV durable flexible OSCs, serving as a built-in UV filter to impede an inevitable UV-induced degradation in ITO-based OSCs.

Keywords: UV durability, flexible organic solar cells, flexible transparent electrode, silver nanowires, hybrid nanostructures

1. Introduction

The development of high performance flexible nonfullerene organic solar cells has attracted considerable attention because of their advantages of high efficiency, mechanical flexibility, and large area solution-fabrication capability at a low cost.[1-3] Encouraging progresses have been made in the development of efficient nonfullerene small molecule acceptors for high efficiency OSCs. The absorption of the nonfullerene acceptors has extended in the near infrared (NIR) region. The NIR absorbing nonfullerene acceptor has been used for application in NIR visualizing device, which comprises of a perovskite light-emitting diode unit and polymer/nonfullerene transparent NIR OSC unit.[4] Very recently, a novel NIR and visible light dual-mode photomultiplication organic photodetector has also been reported.[5] The performance of the OSCs, based on the emerging efficient nonfullerene small molecule acceptors, [6,7] is dependent on the morphology, stratification in bulk heterojunction and the molecular weight of the polymers. It was reported recently that the thermodynamic interaction of polymers and nonfullerene small molecule acceptors is very repulsive. It is fundamentally important for quenching the morphology of the nonfiullerene systems, and thereby improving reliability and stability of the OSCs.[8] Flexible transparent electrodes (FTEs) with superior electric conductivity, high optical transparency and mechanical flexibility are the prerequisites for application in flexible OSCs. [9-11] Indium-tin-oxide (ITO) is a widely used transparent electrode, but it is rigid and cannot be used in flexible OSCs.[12] A variety of FTEs was proposed to replace ITO such as: metallic nanostructures (*e.g.*, nanowires, grids),[13,14] carbon-based materials (*e.g.*, nanotubes, graphene) [15,16] and conducting polymers.[17] Among them, a layer of silver

nanowires (AgNWs) is one of the most promising candidates as an alternative FTE for use in flexible optoelectronic devices because of its superior optical and electric properties.[18-20] However, AgNW-based FTEs still face some technical challenges: first, the randomly distributed AgNWs formed during the solution process result in a large surface roughness that may penetrate through the active layer, leading to electric shorts; second, percolation of charges through junctions between AgNWs results in large contact resistance. The tensile deformation also leads to the irreversible detachment of the NWs at the junctions. As a result, the production of highly conductive and flexible AgNW-based electrode is still one of the open challenges for efficient OSCs. Different approaches were attempted to address this issue. For instance, AgNWs were embedded in the polymer matrix following with a thermal annealing or a high pressure pressing to reduce the surface roughness.[21,22] Different nanoparticles (NPs) were added to fill in the empty spaces between the AgNWs, leading to a decrease in the sheet resistances (*Rs*).[23,24] FTEs incorporating two-dimensional (2D) graphene sheets in AgNW-based FTEs were proposed. The use of graphene sheets helps to reduce the surface roughness and improves the mechanical stability, taking advantage of the 2D graphene pathways for enhancing charge transfer and stretchability of graphene.[25-28] The application of such FTEs has made some initial progresses in the flexible OSCs, however, more improvement is needed.

In parallel to enhance the operation stability of the OSCs, the UV durability is another critical factor for applications in flexible OSCs.[29-31] Deterioration in the performance of the flexible OSCs due to the moisture encroachment and oxidation at the organic electrode interfaces can be minimized by proper encapsulation. The use of the graphene sheets, serving as an oxidation-resistant layer, helps to protect the AgNWs, and thereby improving the stability of AgNWs-based FTEs.[32,33] It is well known that OSCs are unstable under UV irradiation, [34,35] however, the development of UV durable flexible nonfullerene OSCs has not yet been systemically studied.

In this work, we report our effort to develop a high-performance UV durable flexible nonfullerene OSCs realized by incorporating a novel hybrid nanostructured FTE, comprising a mixture of 0D AgNPs, 1D AgNWs and 2D exfoliated graphene (EG) sheets. The all-solution processable hybrid nanostructured FTE has a low sheet resistance of 23 ohm sq^{-1}, a high optical transparency of 82% over the visible light wavelength range and a superior mechanical flexibility.

The flexible OSCs, made with a blend system of poly[(2,6-(4, 8-bis(5-(2-ethylhexyl)thiophen-2-yl)-benzo[1,2-b:4,5-b']dithiophene))-alt-(5,5-(1',3'-di-2-thienyl-5 ',7'-bis(2-ethylhexyl)benzo[1',2'-c:4',5'-c'] dithiophene-4,8-dione)] (PBDB-T): 3,9-bis(2-methylene-(3-(1,1-dicyanomethylene)-indanone))-5,5,11,11-tetrakis(4-hexylphenyl)-dithieno[2,3-d:2',3'-d']-s-indaceno[1,2-b:5,6-b'] dithiophene (ITIC), possess an average power conversion efficiency (PCE) of 8.15% and retain > 90% of the initial PCE after a test of 1000 bends at a radius of 4.0 mm. A significant enhancement in the UV stability of the flexible OSCs has been obtained under a UV-assisted acceleration aging test, arising from the tailored absorption of the hybrid nanostructured FTEs in wavelength < 380 nm.

2. Results and Discussions

A schematic fabrication process of the hybrid nanostructured FTEs is shown in **Figure 1**a. A layer of AgNWs:AgNPs was first coated on the poly(methyl methacrylate) (PMMA)-coated polyethylene terephthalate (PET) substrates, forming a network of AgNWs:AgNPs embedded in the PMMA, which was flattened by a post mechanical pressing process. A layer of EG sheets was then overlaid on the surface of the AgNWs:AgNPs matrix forming a hybrid nanostructured FTE. The scanning electron microscopy (SEM) and atomic force microscopy (AFM) images measured for the surface of AgNWs:AgNPs embedded in the PMMA are shown in **Figures 1**b and **1**(c). It shows that the AgNWs with a diameter of 80 nm and a length of 20-30 μm were randomly distributed forming an AgNW network. AgNPs with a diameter of 60 nm, distributed randomly across the AgNWs, in **Figure 1**b.

In a related work, we have demonstrated that incorporation of gold NPs in the hole transporting layer (HTL) helps to improve the adhesion at the anode/organic interface, and also helps to enhance the charge extraction and reduce the leakage current by improvement of contact property.[36] The use of the AgNPs is to enhance the adhesion between the EG sheets and electric conductivity in the hybrid nanostructured FTEs. The surface morphology is another important FTE parameter for use in flexible OSCs. In this work, the AgNWs:AgNPs were partially embedded in PMMA with a root-mean-square (RMS) roughness of ~17.2 nm, which is obviously lower than that of the pristine AgNWs formed on PET substrate (RMS 28.5 nm). Some pinholes, seen in **Figure 1**c and **Figure S1**

in Supporting Information (SI), were observed on the surface of AgNWs:AgNPs embedded PMMA, which were formed due to the solvent evaporation during the annealing process.

A layer of EG sheets was coated on the AgNWs:AgNPs surface to enhance the mechanical flexibility of FTEs. Comparing to the graphene grown by CVD, [37] EG dispersion has advantages of low-cost, solution-processing and large-scale production, a promising process option for application in flexible OSCs. EG layer also has a lower density of defects as compared to that of the reduced graphene oxide (rGO), leading to an improved electric conductivity.[38] In this work, the layer quality of the EG sheets was evaluated and optimized by using spray coating. Spray coating was adopted because of its potential for producing large area uniform EG film.[39] SEM and AFM images measured for the EG films deposited on ITO substrates are shown in **Figure S1** in SI, having a smooth surface with a RMS of < 3.7 nm. Raman spectra measured for the EG film are shown in **Figure 1**d, the intensity of the G peak (~1580 cm^{-1}) (I_G) is much higher than that of the D peak (I_D). The ratio of I_D to I_G (I_D/I_G) is 0.24, which is much smaller than that measured for an rGO layer (1.1-1.5).[40] The 2D peak at a wavenumber of ~2700 cm^{-1} is clearly visible. This suggests that the EG layer thus prepared has a high graphene quality, despite the presence of a small defect-induced D peak (~1350 cm^{-1}), caused by the edges of the graphene flakes.[41] A small ratio of I_D/I_G of 0.22 was obtained for AgNWs:AgNPs/EG FTEs, confirming the high quality EG film on AgNWs:AgNPs. Comparing to the pristine EG film, the enhanced peak intensity in the Raman spectra, measured for AgNWs:AgNPs/EG, is closely associated with the surface enhanced Raman scattering induced by Ag nanostructures.[42] AFM image measured for the AgNWs:AgNPs/EG is shown in **Figure 1**e. It reveals that EG sheets are uniformly overlaid on the AgNWs, resulting in a low RMS of 6.6 nm as compared to that of the AgNWs:AgNPs surface (RMS 17.2 nm). The height of AgNWs also decreases significantly, as illustrated by the white circles in **Figures 1**c and **1**e. SEM images measured for the AgNW samples with full and partial EG coverages are shown in **Figure S2** in SI. AFM and SEM measurements revealed clearly that the EG sheets were uniformly coated on the surface of the AgNWs:AgNPs interpenetrating networks. The hybrid nanostructured FTE with a smooth surface is favorable for high performance flexible OSCs.

There is an inverse correlation between the optical transparency and *Rs* of the FTEs, which is highly dependent on the fabrication process.[43] The optical transparency and *Rs* measured for

different hybrid nanostructured FTEs are shown in **Figures 2**a and **2**b. An optimal FTE of the bare AgNWs embedded in PMMA had a R_s of 47 ohm sq^{-1} and an average transparency of ~ 87% over the visible light wavelength range from 400 to 800 nm. A slightly lower average transparency of 86% and a lower R_s of 33 ohm sq^{-1} were observed when the AgNPs were incorporated in the AgNWs FTEs. The visible light transparency of the hybrid AgNWs:AgNPs FTE decreased to ~81% after a uniform layer of the EG sheets was coated on its surface, leading to a further decrease in R_s (23 ohm sq^{-1}). The use of a few (2-3) layers of the 2D EG sheets helps to bridge the empty spaces among the AgNWs, leading to an obvious increase in the lateral conductivity and a slight decrease in the optical transparency of the AgNWs:AgNPs/EG FTEs. To better assess the performance of the transparent electrode, the figure of merit (FoM), defined as the ratio of the electric conductivity to optical transparency, is used for analyzing the optical and electric properties of the FTEs. The value of the FoM of the FTEs is calculated using the following equation:[44]

$$\mathrm{FoM} = \frac{188.5}{Rs(T(\lambda)^{-0.5}-1)} \quad (1)$$

where $T(\lambda)$ is the optical transparency of the FTEs measured at 550 nm. The FoM values of 57, 71 and 79 are obtained for different FTEs of AgNWs, AgNWs:AgNPs and AgNWs:AgNPs/EG, calculated using **Equation 1**, the results are plotted in **Figure 2**b.

It is clear that an optimized hybrid nanostructured AgNWs:AgNPs/EG FTE possesses the highest FoM, revealing its suitability for application in flexible OSCs. The mechanical flexibility of the hybrid nanostructured FTEs was examined over 1000 bending cycles, with a radius of 4.0 mm, in the bending test. The ratio of R_s to the initial sheet resistance (R_0) of R_s/R_0 as a function of the bending cycles and aging time was characterized for the hybrid nanostructured FTEs with and without the EG overlayer. The ratios of R_s/R_0 as a function of the number of the bending cycles measured for different FTEs are plotted in **Figure 2**c. It shows that R_s/R_0 value measured for the AgNWs was 4.7 times higher than that obtained for the AgNWs:AgNPs/EG over a test of 1000 bends. The initial R_s values of different FTEs of AgNW, AgNWs/EG and AgNWs:AgNPs/EG were 47, 33, and 23 ohm sq^{-1}, respectively. They increased to 329, 66 and 34.5 ohm sq^{-1}, respectively, after a test of 1000 bends. It reveals that the AgNPs serve as a binding medium assisting in enhancing the adhesion between the AgNWs and EG sheets in the FTEs.

The adhesion between the functional layers in OSCs has been tested and quantified using pull-off forces in the AFM measurements.[45] The force-displacement depicting different cantilever-surface engagements was used to analyze the adhesion in organic electronic devices. In this work, we adopted the similar approach to study the nanoscale adhesion between FTE structure and substrate. In the AFM measurements, AFM tip measured the pull-off force at the FTE/PET interface. The adhesion in the FTE was tested using the pull-off forces in the AFM measurements for estimating the adhesion variation in different FTEs. The adhesion between EG sheets and AgNWs with and without the presence of AgNPs was analyzed using different AFM tip-surface contact forces. AFM tip measures the pull-off force at the EG/AgNW interface, as illustrated in **Figure S3** in SI, while the adhesion is estimated using the pull-off forces. An adhesion force of 20.2 nN was observed for the AgNWs:AgNPs/EG FTE, which is > 25% stronger than the one between EG sheets and AgNWs in the AgNWs /EG FTE, as shown in **Figure S3** in SI. The AFM adhesion measurements support our previous results in showing that the addition of the metal NPs[36] helps to enhance the adhesion between EG sheets and AgNWs in the hybrid nanostructured FTEs.

The stability of the hybrid nanostructured FTEs was analyzed by monitoring the change in the ratio of R_s/R_0 of the FTEs as a function of the aging time, aged over a period of 30 days in air, as shown in **Figure 2**d. The advantages of incorporation of EG sheets and AgNPs in the hybrid FTEs are clearly manifested. The pristine AgNW FTE suffers from an unavoidable oxidation of the AgNWs in air, resulting in an obvious increase in R_s. In contrast, the AgNWs:AgNPs/EG FTEs had a negligible change in R_s during the aging test. It is clear that the use of an upper EG layer acts as an effective barrier layer to prevent the encroachment of the moisture and oxygen, suppressing the oxidation of AgNWs. SEM images measured for the AgNWs FTEs also support above discussion, showing the broken AgNW segments in the bare AgNWs-based FTE due to an unavoidable oxidation of the AgNWs, seen in **Figure S4** in SI. In comparison, AgNWs in AgNWs/EG remained the same morphology. Our results suggest that the incorporation of the EG sheets and AgNPs in the hybrid FTEs has two advantages: (1) it helps to improve the barrier properties, and (2) it enhances the adhesion between the AgNWs and EG sheets, resulting in the hybrid nanostructured FTE with superior flexibility and electric conductivity.

Absorption spectra measured for the different layers of AgNWs, AgNWs:AgNPs,

AgNWs:AgNPs/EG, PBDB-T:ITIC and ITO are shown in **Figure 3**. It becomes clear that the hybrid nanostructured AgNWs:AgNPs/EG FTE has a strong absorption over a short wavelength range with a peak located at ~360 nm, as compared to that of the ITO/glass substrate. The AgNWs:AgNPs/EG FTE has a weak absorption over the visible light wavelength range from 480 to 720 nm. The absorption profile of the AgNWs:AgNPs/EG FTE matches well with the absorption of PBDB-T:ITIC blend layer. It allows the visible light passing through for maximum absorption in the PBDB-T:ITIC bulk heterojunction (BHJ) layer, and prevents the UV part of the incident light entering to the organic active layer. The UV absorption behaviors of the pristine AgNW, AgNW:AgNP and AgNW:AgNPs/EG structures were analyzed using Comsol Multiphysics, as shown in **Figure S5**a in SI. The corresponding distributions of the electric field, calculated by Comsol Multiphysics, are plotted in **Figures S5**b, **S5**c and **S5**d in SI. The calculated absorption, shown in Figure S5a in SI, reveal that there is a slight increase in the absorption of the AgNW:AgNPs/EG structure, particularly over the wavelength range from 300 nm to 600 nm. The simulation supports the experimental results in showing that an improved UV stability of the flexible OSCs with an AgNW:AgNPs/EG-based FTE was observed, due to the improved UV filtering effect as compared to the ones with the AgNW- and AgNW:AgNP-based FTEs. As a result, the use of the AgNWs:AgNPs/EG FTE has an additional advantage, serving as a built-in UV filter for improving the UV durability of the flexible OSCs.

To investigate the feasibility of hybrid nanostructured FTEs for application in flexible OSCs, a set of flexible OSCs comprising a layer configuration of PET/FTEs/poly (3, 4-ethylenedioxy-thiophene) doped with poly (styrenesulfonate) (PEDOT:PSS) (40 nm)/PBDB-T:ITIC (100 nm)/8-hydroxyquinolinolato-lithium (Liq) (1 nm)/Al (100 nm) was fabricated. A 40 nm thick PEDOT:PSS HTL was used to assist in the hole extraction. The use of the bilayer Liq/Al cathode was to improve the electron collection. The flexible OSCs had a 100 nm thick PBDB-T:ITIC BHJ active layer, with an effective active area of 4 mm^2. The current density–voltage (J–V) characteristics measured for the flexible OSCs with different FTEs, under AM1.5G (100 mW/cm^2), are plotted in **Figure 4**b. A summary of the short circuit current density (J_{sc}), open circuit voltage (V_{oc}), fill factor (FF) and PCE is listed in **Table 1**. The control OSC comprising a layer configuration of glass/ITO/PEDOT:PSS (40 nm)/PBDB-T:ITIC (100 nm)/(Liq) (1 nm)/Al (100 nm) was also fabricated for comparison study.

The flexible OSCs with a bare AgNWs FTE had an average PCE of 7.2%, J_{sc} of 12.35 mA cm^{-2}, V_{oc} of 0.89 V, and FF of 65.64%. The one with an AgNWs:AgNPs FTE had an increased PCE of 7.66%, with J_{sc} of 12.74 mA cm^{-2}, V_{oc} of 0.88 V and FF of 67.96%. The improvements in the cell performance are closely associated with the use of the AgNWs:AgNPs FTE, which has a higher conductivity as compared to that of the AgNWs FTE. The average PCE of 8.15% was obtained for the flexible OSCs with an AgNWs:AgNPs/EG FTE, along with a J_{sc} of 13.36 mA cm^{-2}, a V_{oc} of 0.89 V, and a FF of 68.55%. An obvious enhancement in the cell performance agrees well with the discussion on the unique features of the AgNWs:AgNPs/EG FTE, demonstrating its advantages for application in flexible OSCs. A slight deviation in V_{oc} in different OSCs was observed, which is within the experimental error for cells prepared in different batches. The performance of the flexible OSCs made with the solution-processed AgNWs:AgNPs/EG FTE is comparable to that of a control cell with an ITO anode, as shown in **Table 1**.

The external quantum efficiency (EQE) spectra measured for the flexible OSCs with different FTEs are plotted in **Figure 4**c. A broadband enhancement in EQE is observed in the flexible OSCs with an AgNWs:AgNPs/EG FTE as compared to the ones made with AgNWs and AgNWs:AgNPs FTEs. The EQE results consist with the *J–V* measurements. The maximum J_{sc} of 13.17 mA cm^{-2}, 12.36 mA cm^{-2} and 11.53 mA cm^{-2}, calculated using the EQE spectra measured for the flexible OSCs with different FTEs of AgNWs:AgNPs/EG, AgNWs:AgNPs and AgNWs, are presented in **Figure 4**c. The calculated J_{sc} values agree well with the ones obtained by the *J–V* measurements. These results demonstrate that the AgNWs:AgNPs/EG FTE is a favorable alternative to ITO for use in high performing OSCs.

The photocurrent density (J_{ph}) as a function of the effective voltage (V_{eff}), as shown in **Figure 4**d, was used to analyze the charge extraction in the flexible OSCs prepared using different FTEs, where $J_{ph}=J_l - J_d$, J_l is current density measured under the illumination of AM1.5G, and J_d is the dark current density. The effective voltage $V_{eff} = V_0 - V_a$, where V_0 is the built-in potential and V_a is the applied bias. Under a low V_{eff} (< 0.2 V), the charge recombination increases with the decrease in V_{eff}, therefore not all the photo-generated charge carriers can be collected due to the bimolecular recombination.[46] Under a high V_{eff} (> 0.6 V), almost all the photo-generated charge carriers can be swept out and collected, generating a saturated photocurrent density (J_{sat}). Apparently, J_{ph} measured

for the flexible OSCs with an AgNWs:AgNPs/EG FTE can reach J_{sat} under a lower applied bias as compared to the cells with an AgNWs FTE or AgNWs:AgNPs FTE, as shown in **Figure S6** in SI, indicating a more efficient charge extraction capability in the flexible OSCs made with an AgNWs:AgNPs/EG FTE. The charge collection probability (P_{CC}) can be analyzed using the ratio of J_{ph}/J_{sat}. Under V_{eff} < 0.3 V, a higher P_{CC} is observed for flexible OSCs with an AgNWs:AgNPs/EG FTE as compared to the cells made with a pristine AgNWs contact or an AgNWs/EG FTE, as shown in **Figure 4**d.

The mechanical flexibility of the flexible OSCs made with the AgNWs:AgNPs TFE and AgNWs:AgNPs/EG FTE was studied by a bending test with a radius of 4.0 mm. The results are shown in **Figure 5**. The V_{oc}, J_{sc} and FF of the flexible OSCs with an AgNWs:AgNPs/EG FTE can retain > 96% of their initial values after a test of 1000 bends. While the V_{oc}, J_{sc} and FF of the flexible OSCs with an AgNWs:AgNPs FTE remained only 80%-85% of their initial values, the corresponding PCE of the flexible OSCs with an AgNWs:AgNPs/EG FTE maintained > 90% of their initial efficiency, which is much higher than that of the ones made with an AgNWs:AgNPs FTE (< 60%). The results of the bending tests of the flexible OSCs with two different radii of 2.0 and 4.0 mm are plotted in **Figure S**7 in SI. The flexible OSCs, bended with a radius of 2.0 mm, maintained 81.1% of initial efficiency after 1000 bending cycles, which is slightly lower than that of the flexible cells bended with a radius of 4.0 mm (90.3%). The flexible OSCs, made with an AgNWs:AgNPs/EG FTE, having an average PCE of > 8% are clearly demonstrated.

In a recent work, we have shown that maintaining a stable and high built-in potential across BHJ through interfacial modification favors the efficient and stable operation of OSCs. [47, 48] In addition to the operational stability, the UV durability is another important factor for practical application of OSCs. The UV durability of the flexible OSCs and a control OSC made with an ITO anode was analyzed by exposing the cells to a UV lamp, with a peak wavelength of 360 nm and an intensity of 200 W/m^2, under different UV exposure times. To avoid the possible cell degradation due the moisture and oxygen encroachment, the accelerated UV durable tests were conducted in the N_2-purged glove box with O_2 and H_2O levels < 0.1 ppm. The variation in V_{oc}, J_{sc}, FF and PCE measured for the flexible OSCs under different UV exposure times are compared to that of the control cell, and the results are plotted in **Figure 6**. Although the ITO-based control cell had a

higher initial PCE, a fast decrease in its V_{oc}, J_{sc}, FF and PCE was observed after a 60 min UV exposure. For example, a loss in V_{oc} from 0.89 V to 0.84 V, a decrease in J_{sc} from15.45 mA cm^{-2} to 10.37 mA cm^{-2}, and a reduction in FF from 68.1% to 57.5 % were observed, leading to a 47% drop in PCE from 9.7% to 5%. A slower degradation in the performance of the flexible OSCs with an AgNWs:AgNPs/EG FTE, aged under the same UV exposure condition, has been observed. For example, a mild drop in V_{oc} from 0.89 V to 0.87 V, a smaller decrease in J_{sc} from 13.4 mA cm^{-2} to 11.65 mA cm^{-2} and a lesser reduction in FF from 67.7% to 61.2%, resulting in a smaller decrease of 23% in PCE from 8.15% to 6.20%. It is clear that the flexible OSCs have a superior UV durability as compared to that of a control OSC made with an ITO contact. The enhancement in the UV durability of the flexible OSCs is attributed to the tailored absorption of the AgNWs:AgNPs/EG FTE over the short wavelength range, as shown in **Figure 3**. Apart from the superior mechanical flexibility, electric conductivity and solution fabrication capability, the use of the solution-processable FTE developed in this work aids in further benefit on its tailored absorption in wavelength < 380 nm, offering an exciting option for application in low-cost large area UV durable flexible OSCs.

In addition to the analysis made with the UV stability of the flexible OSCs with a PBDB-T:ITIC blend layer, a series of UV aging tests were conducted for the flexible OSCs prepared using other emerging nonfullerene small-molecule acceptors. [6,7] The normalized PCE as a function of the UV exposure time, measured for a set of the flexible OSCs made with different polymer/nonfullerene acceptor blend systems are plotted in **Figure S**8 in SI. The flexible OSCs made with different blend systems experienced a similar and consistent degradation behavior aged under the same UV exposure condition. It becomes clear that PCE of the control OSCs, made with different blend systems, having an ITO front contact decreases much faster as compared to the ones made with a front hybrid nanostructured FTE, revealing its suitability for attaining an improved UV stable flexible OSCs prepared using different polymer/nonfullerene acceptor systems. Our results demonstrate that the use of the FTE benefits the UV stability of the flexible OSCs, serving as a built-in UV filter to inhibit an inevitable degradation seen in ITO-based OSCs, caused by the UV irradiation.

3. Conclusions

A novel solution-processable hybrid nanostructured AgNWs:AgNPs/EG FTE has been

developed for application in UV durable flexible nonfullerene OSCs. The FTE possesses a high electric conductivity, an excellent mechanical flexibility and chemical stability. An average PCE of 8.15% was obtained for the flexible OSCs made with an AgNWs:AgNPs/EG FTE. The flexible OSCs exhibit an excellent mechanical flexibility, retaining > 90% of the initial PCE after a test of 1000 bending cycles. Most importantly, the flexible OSCs also possess an excellent UV durability as compared to the control OSC made with an ITO anode, taking advantage of the tailored FTE absorption in wavelength < 380 nm. The FTE developed in this work offers an attractive option as an ITO alternative for application in UV durable flexible OSCs.

4. Experimental Section

Material Formulation and FTE Preparation

The solution of AgNWs, with an average diameter of 80 nm and a length of 20-30 μm, was purchased from BlueNano Company. The solution of AgNPs, with an average diameter of 60 nm, was purchased from Sigma Aldrich. EG dispersion in N-Methyl pyrrolidone solution with a concentration of 4 mg mL^{-1} was purchased from XFNANO. The lateral size of EG sheets is over the range from 0.5-3.0 μm, while the layer thickness of the EG sheets is about 0.3-2.0 nm. PBDB-T and ITIC were purchased from Solarmer. The small molecule material Liq was obtained from e-Ray Optoelectronics Corp. PMMA, chlorobenzene and 1,8-diiodooctane were received from Sigma Aldrich. The chemical materials were used as received without further treatment and modification.

The AgNWs:AgNPs/EG FTEs on PET substrates were prepared by an all-solution process, the fabrication route is schematically illustrated in **Figure 1**a. The PET substrates were cleaned by ultrasonication sequentially with detergent, de-ionized water, and isopropanol each for 15 min. Then, PMMA solution (120 mg ml^{-1}) was spin-coated on PET substrates at a rotation speed of 1000 rpm for 60 s, followed by an annealing on a hot plate at 110 ℃ for 10 min to form a supporting layer. Subsequently, a layer of AgNPs:AgNWs was formed on the PMMA-coated PET substrates by spin coating using a mixture solution with a volume ratio of AgNPs to AgNWs of 1:8, following with an annealing at 110 ℃ in air for 15 min. An additional mechanical pressure was used for embedding the AgNWs in the PMMA layer. The pressure was loaded by a custom-made compressor controlled by the air pressure. The film was sandwiched between two clean glass substrates and then transferred into the compressor for embedding the AgNWs:AgNPs in the PMMA layer. Finally, EG

dispersion was sprayed on the surface of the AgNPs:AgNWs layer using an airbrush system. An airbrush with a nozzle diameter of 0.3 mm was set in single action mode to fix a ratio of EG to air. The inlet air pressure was set at 1.7 bar. The thickness of the EG layer was controlled by optimizing the spray parameters. The EG dispersion was atomized into small droplets by controlling the airflow, followed by a post deposition annealing at 110 ℃ for 1 min in air to form a continuous film.

Device Fabrication and Characterization

PEDOT:PSS HTL was deposited on the FTE/PET substrate via a spin-coating at 3000 rpm for 60 s, followed by an annealing at 110 ℃ for 30 min in air. A 100 nm thick organic active layer was formed on the PEDOT:PSS surface by spin-coating at 1750 rpm for 60 s in glove box with O_2 and H_2O levels < 0.1 ppm, using a blend of PBDB-T:ITIC (1:1) in chlorobenzene and 1,8-diiodoctane (99.5:0.5 by volume) with a total concentration of 20 mg ml^{-1}. Finally, a 2×2 mm sized bilayer Liq (~1.0 nm)/Ag (100 nm) cathode, defined by the shadow mask, was deposited sequentially on the active layer by thermal evaporation in a vacuum system, with a base pressure of < 10^{-6} Pa. Liq was deposited at rate of 1.0 Å s^{-1}, while Al was deposited at a rate of 5.0 Å s^{-1}.

The surface morphology of the AgNWs:AgNPs/EG FTEs was analyzed using SEM (HITACHI S-4800) and AFM (Nanonavi SPA-400SPM) measurements. The Raman spectroscopy measurements were carried out using a Horiba LabRam spectrometer with a 473 nm laser excitation source. A 100x objective (NA 0.9) was used, having a spatial resolution < 1.0 μm. The optical transparency and the absorption spectra of the FTEs were measured using a UV-vis spectrophotometer (HITACHI Ue3900H). The R_s of different FTEs was measured using a 4-point probe system (RS8, BEGA Technologies). The *J–V* characteristics of the OSCs were measured using a calibrated AM 1.5G solar simulator (ABET Sun2000) (100 mW/cm^2). EQE spectra of the OSCs were measured using a 7-SCSpec solar cell measurement system (7-STAR Co.). The OSCs were not encapsulated, the measurements were conducted in air.

The adhesion between the EG sheets and the AgNWs with and without the presence of the AgNPs in the FTEs was characterized using the AFM force mapping (Nanoscope Analysis v1.80, Bruker). PFQNM-LC-A-CAL probes (Bruker) with a spring constant ranging from 0.07 N/m to 0.1 N/m, a tip radius of curvature of 65 nm, and a tip half-angle of 18° were applied in the adhesion measurements. The adhesion measurements were conducted in vacuum to reduce the noise.

Force-distance mappings were acquired using a loading force of 1.0 nN, providing an indentation range from 200 to 500 nm. Modulus and adhesion signal channel were used to display the cell force mapping.

Theoretical Simulation

Absorption spectra and distributions of the electric-field amplitude of a pure AgNW, having a diameter of 80 nm and a length of 3.5 μm, and the one grouped with ten 60 nm-sized spherical AgNPs were calculated using Comsol Multiphysics. A model of a 1.0 nm thick multilayer EG embedded in the AgNW and AgNPs was proposed for the AgNW:AgNPs/EG structure in the simulation. The corresponding absorption spectrum and distribution of the electric-field amplitude were calculated using the optical constants of graphene layer in the visible wavelength range.[49] In the calculation, we considered incident planewave normal to the AgNW/glass substrate or AgNW:AgNPs/glass substrate, polarized perpendicular to the NW's axis. The assumption of the perfectly matched layers was used in the calculation, and symmetries were used to optimize memory and computation time.

Supporting Information

Supporting Information is available from the Wiley Online Library or from the author.

Acknowledgements

This work was financially supported by the National Natural Science Foundation of China (61775130, 11974236), Natural Science Foundation of Shanghai (19ZR1419500), Research Grants Council, University Grants Committee of Hong Kong Special Administrative Region, China, General Research Fund (GRF/12302419), Collaborative Research Fund (C5037-18GF), NSFC/RGC Joint Research Scheme (N_HKBU201/19) and Hong Kong Baptist University Inter-institutional Collaborative Research Scheme (RC-ICRS/15-16/04).

Conflict of Interest

There are no conflicts to declare.

References

[1] P. Cheng, G. Li, X. Zhan, Y. Yang, *Nat. Photonics*. **2018**, *12*, 131.

[2] J. Hou, O. Inganas, R. H. Friend, F. Gao, *Nat. Mater*. **2018**, *17*, 119.

[3] Y. B. Cheng, A. Pascoe, F. Huang, Y. Peng, *Nature*. **2016**, *539*, 488.

[4] N. Li, Y. S. Lau, Z. Xiao, L. M. Ding, F. R. Zhu, *Adv. Opt. Mater*. **2018**, *6*, 1801084.

[5] Z. J. Lan, Y. L. Lei, W. K. Chan, S. M. Chen, D. Luo, F. R. Zhu, *Sci. Adv*. **2020**, *6*, eaaw8065.

[6] J. Zhang, H. S. Tan, X. Guo, A. Facchetti, H. Yan, *Nat. Energy.* **2018**, *3*, 720.

[7] L. Ye, H. Hu, M. Ghasemi, T. Wang, B. A. Collins, J. H. Kim, K. Jiang, J. H. Carpenter, H. Li, Z. K. Li, T. McAfee, J. Zhao, X. Chen, J. Lai, T. Ma, J. L. Bredas, H. Yan, H. Ade, *Nature Mater*. **2018**, *17*, 253.

[8] L. Ye, S. Li, X. Liu, S. Zhang, M. Ghasemi, Y. Xiong, J. Hou, H. Ade, *Joule*. **2019**, *3*, 1.

[9] Y. Q. Li, L. W. Tan, X. T. Hao, K. S. Ong, F. R. Zhu, L. S. Hung, *Appl. Phys. Lett*. **2005**, *86*, 153508.

[10] H. Wu, D. Kong, Z. Ruan, P. C. Hsu, S. Wang, Z. Yu, T. J. Carney, L. Hu, S. Fan, Y. Cui, *Nat. Nanotechnol.* **2013**, *8*, 421.

[11] S. L. Wang, Y. Zhao, H. Lian, C. Peng, X. Yang, Y. Gao, Y. Peng, W. Lan, O. Ibrahim Elmi, D. Stiévenard, B. Wei, F. R. Zhu, T. Xu, *Nanophotonics*. **2019**, *8*, 297.

[12] R. Peng, W. Song, T. Yan, B. Fanady, Y. B. Li, Q. F. Zhan, Z. Y. Ge, *J. Mater. Chem. A.* **2019**, *7*, 11460.

[13] A. Kim, Y. Won, K. Woo, S. Jeong, J. Moon, *Adv. Funct. Mater*. **2014**, *24*, 2462.

[14] C. Peng, C. Chen, K. P. Guo, Z. H. Tian, W. Zhu, T. Xu, B. Wei, *Physica E*. **2017**, *7*, 118.

[15] J. Y. Kim, Y. J. Park, *Sci. Reports.* **2017**, *7*, 8610.

[16] K. S. Kim, Y. Zhao, H. Jang, S. Y. Lee, J. M. Kim, K. S. Kim, J. H. Ahn, P. Kim, J. Y. Choi, B. H. Hong, *Nature.* **2009**, *457*, 706.

[17] M. H. Lee, L. X. Chen, N. Li, F. R. Zhu, *J. Mater. Chem. C*, **2017**, *5*, 10555.

[18] J. Y. Lee, S. T. Connor, Y. Cui, P. Peumans, *Nano Lett.* **2008**, *8*, 689.

[19] L. Yang, T. Zhang, H. Zhou, S. C. Price, B. J. Wiley, W. You, *ACS Appl. Mater. Interfaces*. **2011**, *3*, 4075.

[20] Y. X. Zhang, J. Fang, W. Li, Y. Shen, J. D. Chen, Y. Q. Li, H. W. Gu, S. Pelivani, M. J. Zhang, Y. F. Li, J. X. Tang, *ACS Nano.* **2019**, *13*, 4686.

[21] Y. Kim, T. I. Ryu, K. H. Ok, M. G. Kwak, S. Park, N. G. Park, C. J. Han, B. S. Kim, M. J. Ko, H. J. Son, J. W. Kim, *Adv. Funct. Mater*. **2015**, *25*, 4580.

[22] W. Xiong, H. Liu, Y. Chen, M. Zheng, Y. Zhao, X. Kong, Y. Wang, X. Zhang, X. Kong, P. Wang, L. Jiang, *Adv. Mater.* **2016**, *28*, 7167.

[23] T. Kim, S. Kang, J. Heo, S. Cho, J. W. Kim, A. Choe, B. Walker, R. Shanker, H. Ko, J. Y. Kim, *Adv. Mater*. **2018**, *30*, 1800659.

[24] B. Wei, S. Pan, T. Wang, Z. Tian, G. Chen, T. Xu, *Nanotechnol.* **2016**, *27*, 505208.

[25] N. Ye, T. Liang, L. Zhan, Y. Kong, S. Xie, X. Ma, H. Chen, H. Su, M. S. Xu, *IEEE J. Photovoltaic.* **2019**, *9*, 214.

[26] A. G. Ricciardulli, S. Yang, G. A. H. Wetzelaer, X. Feng, P. W. M. Blom, *Adv. Funct. Mater*. **2018**, *28*, 1706010.

[27] X. Zhang, J. Wu, H. Liu, J. Wang, X. F. Zhao, Z. Y. Xie, *Org. Electron.* **2017**, *50*, 255.

[28] Z. Y. Liu, Z. S. Wu, S. Yang, R. H. Dong, X. L. Feng, K. Mullen, *Adv. Mater.* **2016**, *28*, 2217.

[29] H. X. Liu, Z. H. Wu, J. Q. Hu, Q. L. Song, B. Wu, H. L. Tam, Q. Y. Yang, W. H. Choi, F. R.

Zhu, *Appl. Phys. Lett*. **2013**, *103*, 043309.

[30] X. Z. Wang, C. X. Zhao, G. Xu, Z. K. Chen, F. R. Zhu, *Sol. Energy Mater. Sol. Cells.* **2012**, *104*, 1.

[31] C. Vijila, G. M. Ng, M. J. Tan, W. P. Goh, F. R. Zhu, *Appl. Phys. Lett*. **2009**, *95*, 263305.

[32] I. N. Kholmanov, S. H. Domingues, H. Chou, X. H. Wang, C.g Tan, J. Y. Kim, H. F. Li, R. Piner, A. J. G. Zarbin, R. S. Ruoff, *ACS Nano*. **2013**, *7*, 1811.

[33] M. S. Lee, K. Lee, S. Y. Kim, H. Lee, J. Park, K. H. Choi, H. K. Kim, D. G. Kim, D. Y. Lee, S. W. Nam, J. U. Park, *Nano Lett*. **2013**, *13*, 2814.

[34] J. Jeong, J. Seo, S. Nam, H. Han, H. Kim, T. D. Anthopoulos, D. D. C. Bradley, Y. Kim, *Adv. Sci.* **2016**, *3*, 1500269.

[35] H. Kimura, K. Fukuda, H. Jinno, S. Park, M. Saito, I. Osaka, K. Takimiya, S. Umezu, T. Someya, *Adv. Mater.* **2019**, *31*, 1808033.

[36] W. D. Zhang, W. X. Lan, M. H. Lee, J. Singh, F. R. Zhu, *Org. Electrons*, **2018**, *52*, 1.

[37] T. Xu, A. Díaz Álvarez, W. Wei, D. Eschimese, S. Eliet, O. Lancry, E. Galopin, F. Vaurette, M. Berthe, B. Wei, J. Xu, J. F. Lampin, E. Pallecchi, H. Happy, D. Vignaud, B. Grandidier. *Nanoscale.* **2018**, *10*, 7519.

[38] Z. L. Luo, Z. P. Cai, Y. B. Wang, Y. P. Wang, B. B. Wang, *RSC Adv*. **2016**, *6*, 37124.

[39] A. G. Riccardulli, S. Yang, X. Feng, P. W. M. Blom, *ACS Appl. Mater. Interfaces*. **2017**, *9*, 25412.

[40] Y. Hernandez, V. Nicolosi, M. Lotya, F. M. Blighe, Z. Sun. S. De, I. T. McGovern, B. Holland, M. Byrne, Y. K. Gun'Ko, J. J. Boland, P. Niraj, G. Duesberg, S. Krishnamurthy, R. Goodhue, J. Hutchison, V. Scardaci, A. C. Ferrari, J. N. Coleman, *Nat. Nanotechnol.* **2008**, *3*, 563.

[41] Y. X. Wang, S. L. Chou, H. K. Liu, S. X. Dou, *Carbon*. **2013**, *57*, 202.

[42] X. J. Wang, C. H. Zhu, X. Y. Hu, Q. L. Xu, H. P. Zhao, G. W. Meng, Y. Lei, *Appl. Surf. Sci*. **2019**, *486*, 405.

[43] X. Zhang, V. A. Öberg, J. Du, J. Liu, E. M. J. Johansson, *Energy Environ. Sci.* **2018**, *11*, 354.

[44] M. Vosgueritchian, D. Lipomi, Z. Bao, *Adv. Funct. Mater*. **2012**, *22*, 421.

[45] T. Tong, B. Babatope, S. Admassie, J. Meng, O. Akwogu, W. Akande, W.O. Soboyejo, *J. Appl. Phys.* **2009**, *106*, 083708.

[46] W. X. Lan, Y. Liu, B. Wu, B. Xu, H. Y. Pu, B. Wei, Y. Peng, W. J. Tian, F. R. Zhu, *ACS Appl. Energy Mater*. **2019**, *2*, 7385.

[47] Y. W. Wang, W. X. Lan, N. Li, Z. J. Lan, Z. Li, J. N. Jia, F. R. Zhu, *Adv. Energy Mater*. **2019**, *9*, 1900157.

[48] Y. W. Wang, B. Wu, Z. H. Wu, Z. J. Lan, Y. F. Li, M. J. Zhang, F. R. Zhu, *J. Phys. Chem. Lett*. **2017**, *8*, 5264.

[49] M. Bruna, S. Borini, *Appt. Phys. Lett.* **2009**, *94*, 031901.

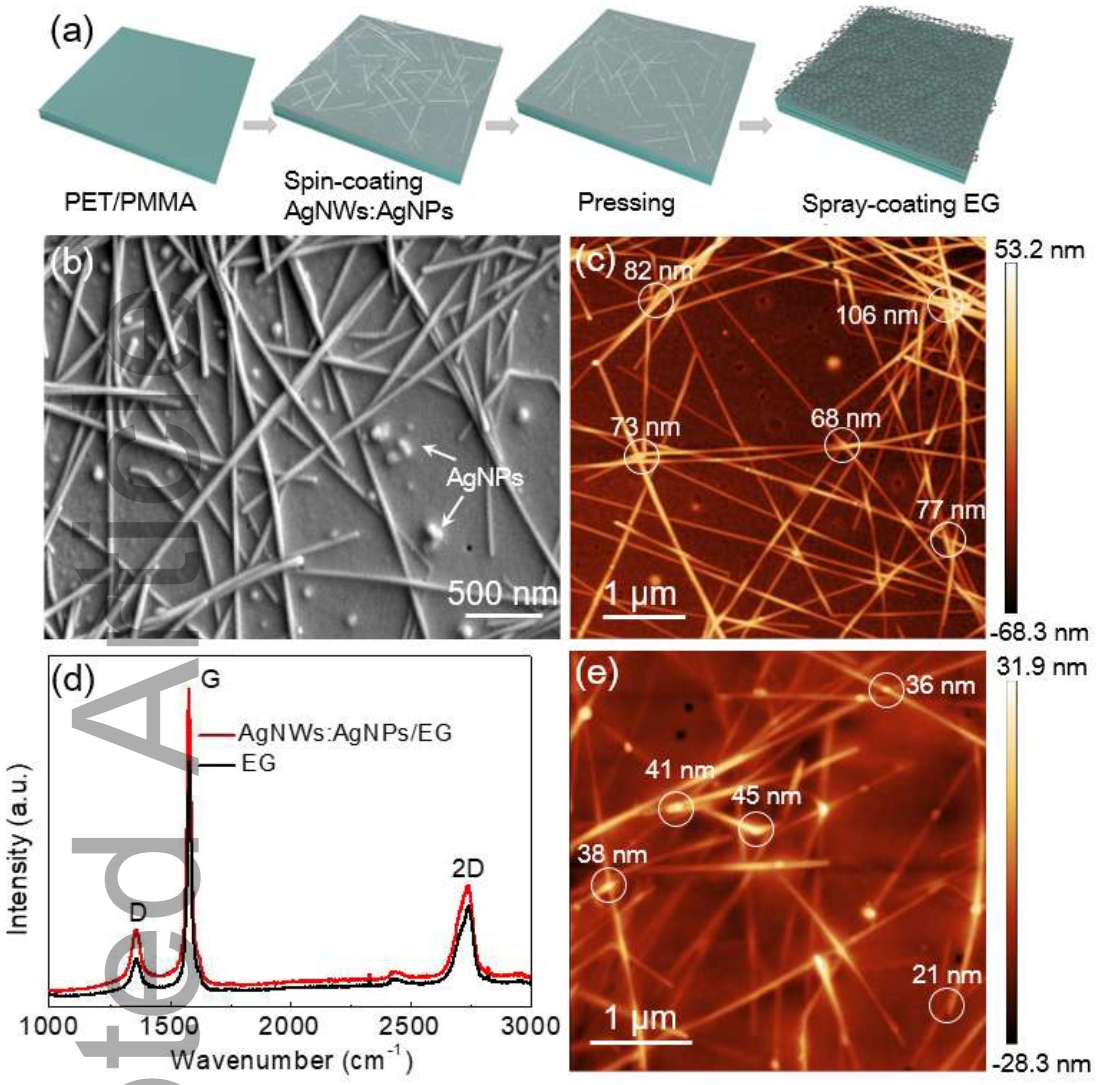

Figure 1. (a) Schematic fabrication process of AgNWs:AgNPs/EG FTE. (b) SEM and (c) AFM images measured for the surface of AgNWs:AgNPs embedded in PMMA. (d) Raman spectrum measured for the EG sheets and AgNWs:AgNPs/EG. (e) AFM image measured for the EG sheets deposited on the AgNWs:AgNPs. The white circles in the AFM images indicate the height of the overlapped AgNWs.

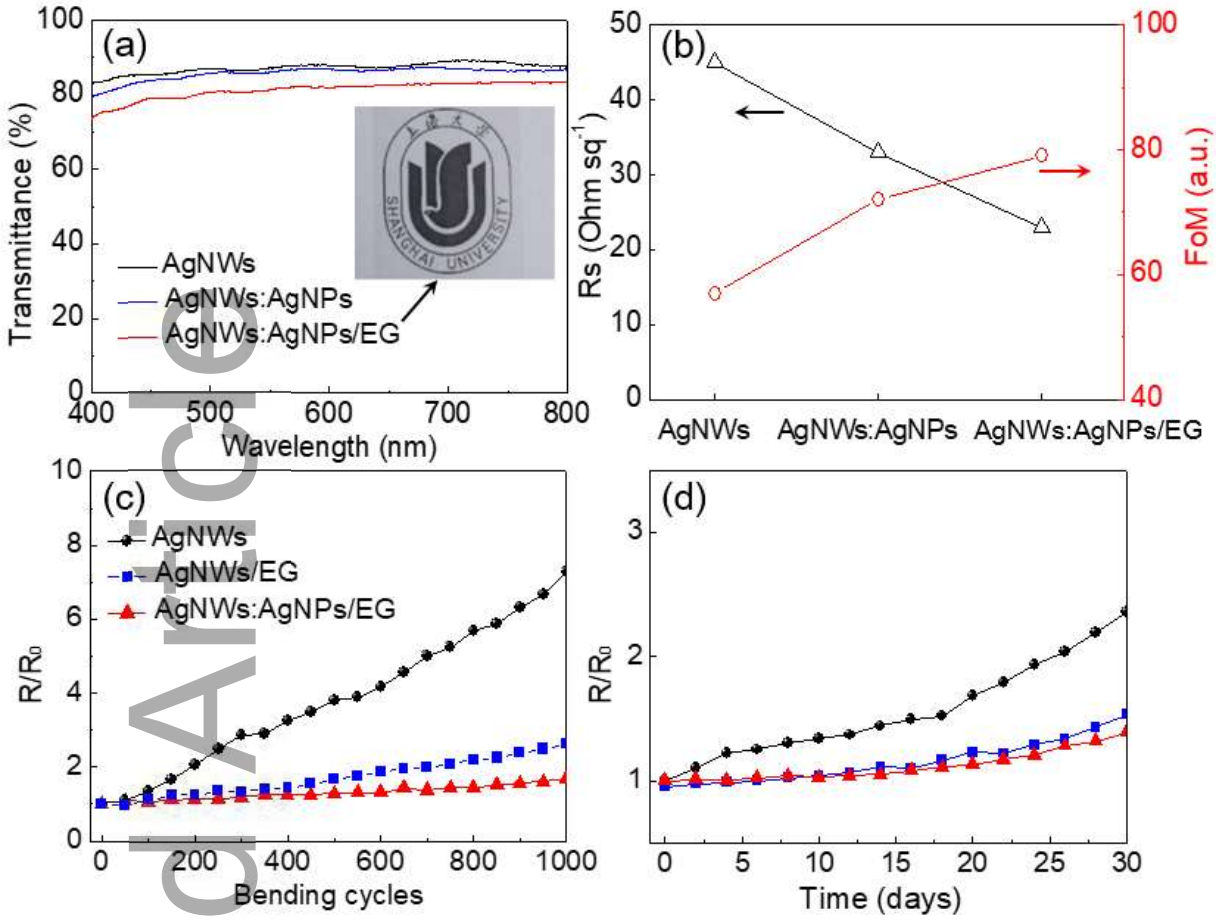

Figure 2. (a) Optical transparency spectra, and (b) sheet resistance and FoM values obtained for different FTEs of AgNWs, AgNWs:AgNPs and AgNWs:AgNPs/EG. Rs/R_0 ratio as a function of (c) the number of bending cycles and (d) aging time for different FTEs of the bare AgNWs, AgNWs/EG and AgNWs:AgNPs/EG. Inset in (a): picture taken for the transparent AgNWs:AgNPs/EG PET substrate placed on top of the university emblem.

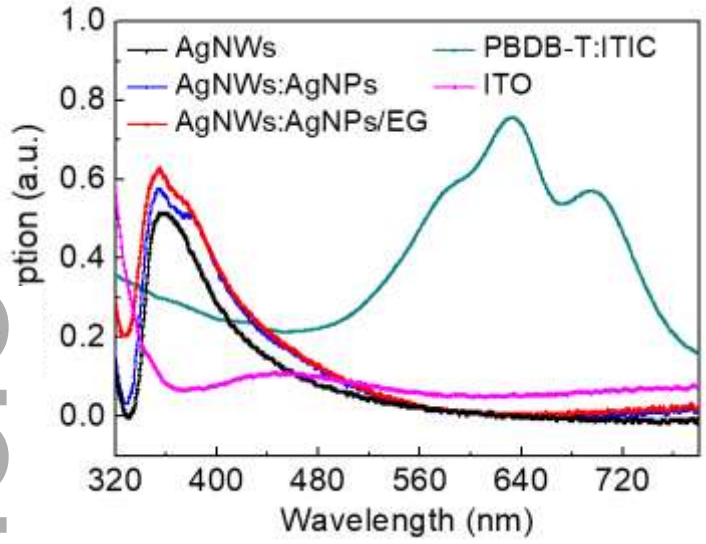

Figure 3. Absorption spectra measured for different layers of AgNWs, AgNWs:AgNPs AgNWs:AgNPs/EG, PBDB-T:ITIC and ITO used in this work.

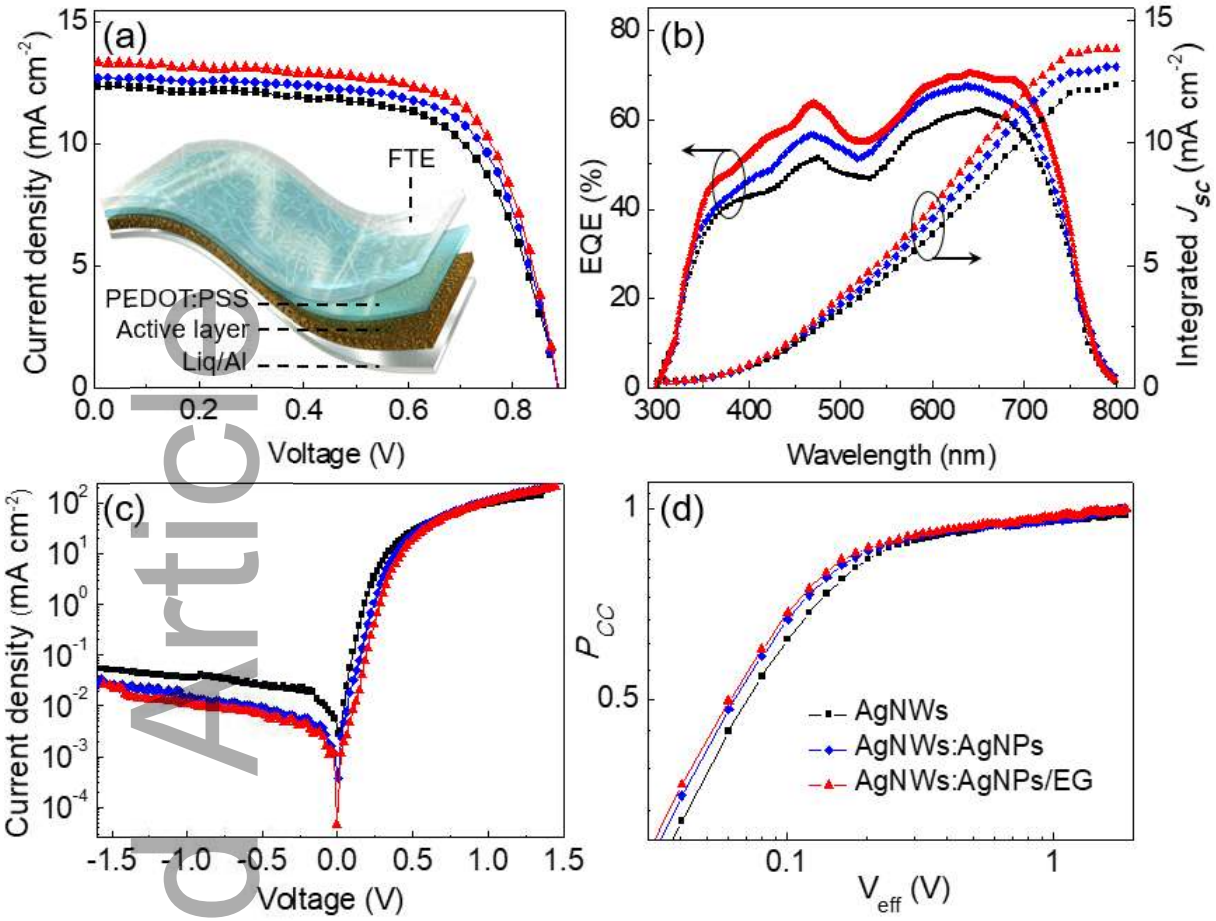

Figure 4. (a) *J–V* characteristics, (b) EQE spectra measured, (c) dark *J–V* characteristics and (d) charge collection efficiency P_{CC} characteristics for the flexible OSCs made with different hybrid nanostructured FTEs of AgNWs, AgNWs:AgNPs and AgNWs:AgNPs/EG. The integrated J_{sc} calculated using EQE for the flexible OSCs with different hybrid nanostructured FTEs are also presented in (c). Inset of (a): schematic layer configuration of the flexible OSCs made with a hybrid nanostructured FTE-coated PET substrate.

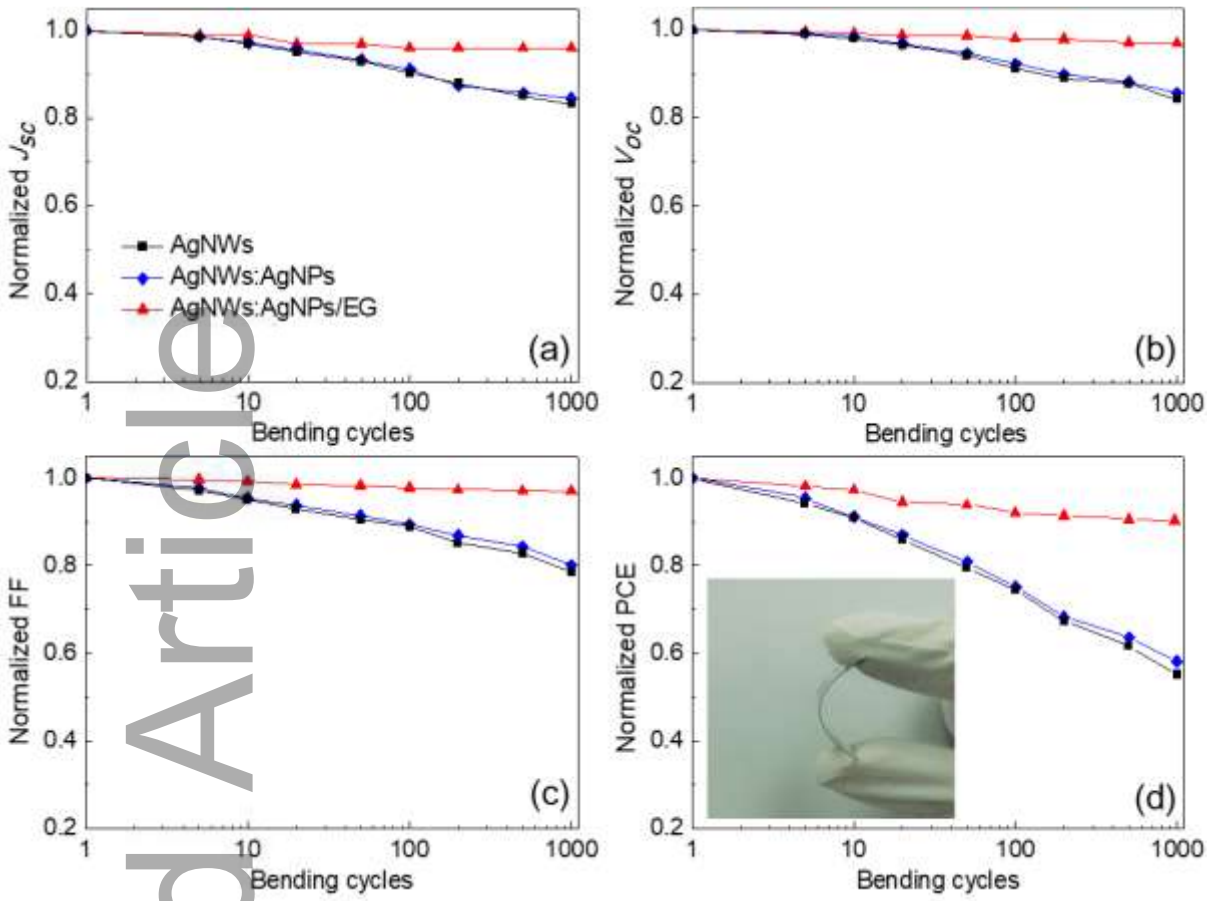

Figure 5. Normalized (a) J_{sc}, (b) V_{oc}, (c) FF and (d) PCE of the flexible OSCs with different FTEs of AgNWs, AgNWs:AgNPs and AgNWs:AgNPs/EG as a function of the number of the bending cycles. Inset in (a): picture taken for a flexible OSC with a AgNWs:AgNPs/EG contact.

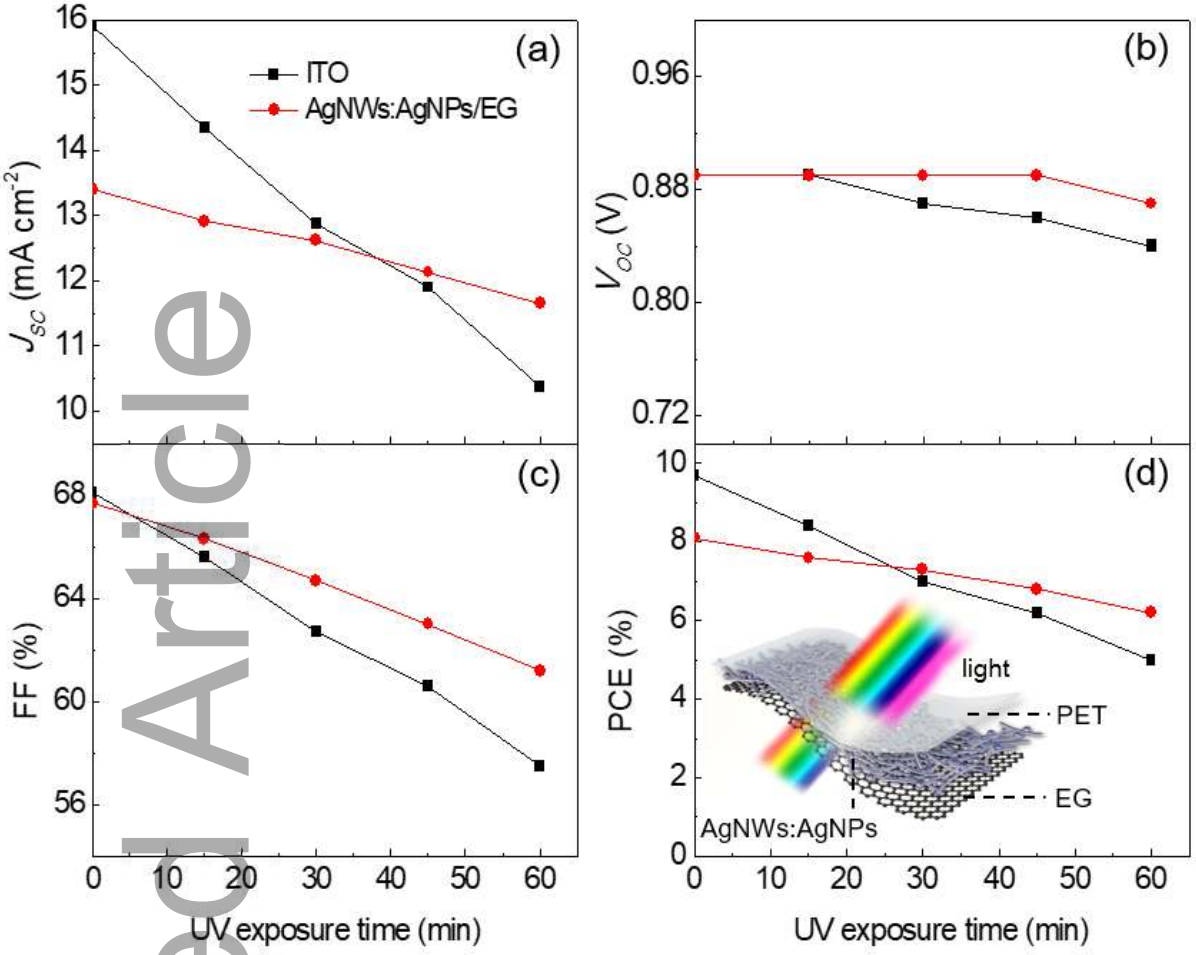

Figure 6. Evolution of (a) J_{sc}, (b) V_{oc}, (c) FF, and (d) PCE measured for a flexible OSC with an AgNWs:AgNPs/EG FTE and a control cell with an ITO anode as a function of the UV exposure time. Inset in (b): schematic view of the FTE filtering the UV portion of the incoming light.

Table 1. A summary of the performance of OSCs made with different transparent electrodes, averaged from >10 cells.

Transparent electrode	V_{oc} (V)	J_{sc} (mA cm^{-2})	FF (%)	Average PCE (Maximum PCE) (%)
AgNWs	0.89	12.35	65.64	7.20 (7.60)
AgNWs:AgNPs	0.88	12.74	67.96	7.66 (7.81)
AgNWs:AgNPs/EG	0.89	13.36	68.55	8.15 (8.32)
ITO	0.89	15.45	68.89	9.51 (9.74)

Table of Contents

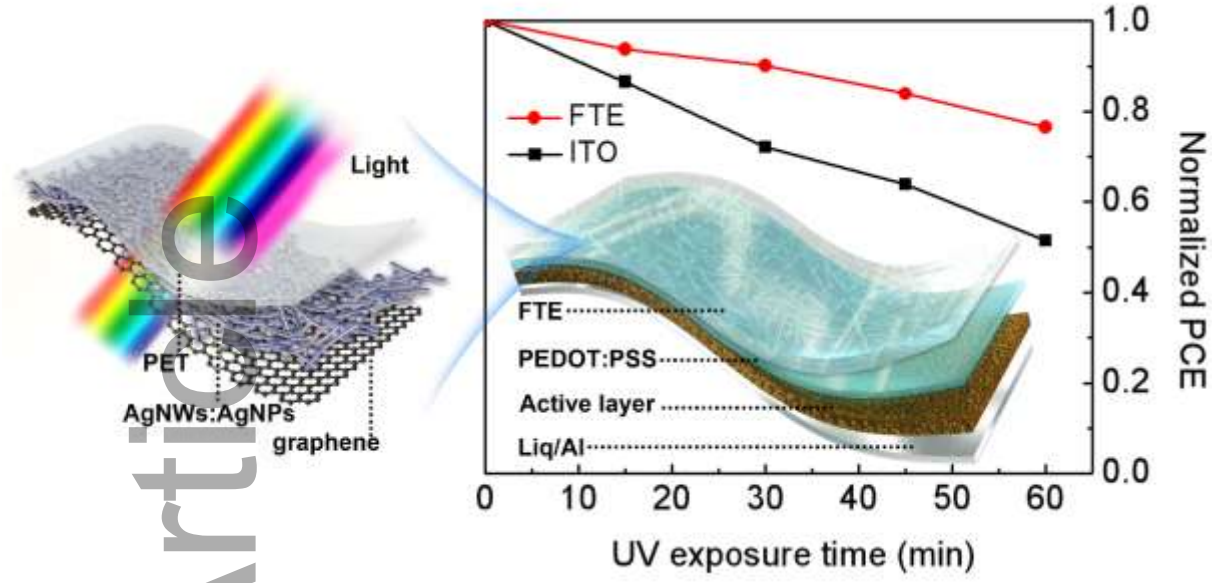

TOC keyword: UV durable organic solar cells

A UV durable ITO-free flexible nonfullerene organic solar cell has been demonstrated, realized by incorporating a hybrid nanostructured flexible transparent electrode with a tailored absorption in wavelength < 380 nm.